Article

Computer-Integrated Surface Image Processing of Hydrogen-Saturated Steel Wear Products

Alexander I. Balitskii [1,2,*], Valerii O. Kolesnikov [1,3], Valentina O. Balitska [4], Ljubomyr M. Ivaskevych [1], Jakub M. Dowejko [5], Bartosz J. Pilecki [5] and Maria R. Havrilyuk [1]

[1] Department of Strength of the Materials and Structures in Hydrogen-Containing Environments, Karpenko Physico-Mechanical Institute, National Academy of Sciences of Ukraine, 5 Naukova Str., 79601 Lviv, Ukraine; kolesnikov@ipm.lviv.ua (V.O.K.); ivaskevich@ipm.lviv.ua (L.M.I.); gavriluk@ipm.lviv.ua (M.R.H.)

[2] Department of Mechanical Engineering and Mechatronics, West Pomeranian University of Technology in Szczecin, 19 Piastow Av., 70-310 Szczecin, Poland

[3] Department of Professional Education Taras Shevchenko National University of Lugansk, Kovalya Str. 3, 36000 Poltava, Ukraine

[4] Department of Physics and Chemistry of Combustion, Lviv State University of Life Safety, 35 Kleparivska, 79000 Lviv, Ukraine; vbalitska@yahoo.com

[5] Institute of Management, University of Szczecin, Cukrowa 8, 71-004 Szczecin, Poland; jakub.dowejko@usz.edu.pl (J.M.D.); bartosz.pilecki@usz.edu.pl (B.J.P.)

* Correspondence: abalicki@zut.edu.pl

Featured Application: Modern robotic approaches to the evaluation of sensitivity to hydrogen embrittlement and the degradation of steel and alloys by wear products.

Abstract: This paper briefly describes the conceptual direction of the application of computer vision (CV) methods that involve controlling the morphology of hydrogenated wear particles (WPs). During long-term operation, in the surface and subsurface layers of the materials of parts in the tribo-joint, changes in the micromechanisms of fracture occur, which change the morphology of WPs. It has been shown that the developed computer program (CP) can be used to monitor the fractography of the surface of wear particles, and, accordingly, it is possible to control changes in the surface morphology. Therefore, it is possible to predict the operational stability and durability of the tribo-joint. A conceptual scheme for determining the performance of a tribotechnical assembly depending on the determined parameters of WPs is presented. The modes marked on it, including normal operation, transient, run-in, and catastrophic failure, can be evaluated by robotics approaches.

Keywords: computer vision; wear particles; hydrogen; fracture

1. Introduction

Under friction conditions, WPs are separated. If the friction mode is normal, the separation of the particles has a fatigue failure mechanism. However, if the friction mode occurs in a "catastrophic mode", the fracture mechanism changes. Wear particles can act as indicators of the change in fracture mechanisms at friction [1–3]. During long-term operation, some parts of tribotechnical assemblies come into contact with hydrogen-containing working media, resulting in the accumulation of hydrogen in their surface and subsurface layers. This affects the micromechanisms of fracture and is manifested in fractographic features, which, due to the development of computer vision methods, can be used to ensure the reliability, durability, and safety of machines and mechanisms [4–7].

Consequently, there is a need to develop and apply modern conceptual mechatronic and robotic systems to create computer-integrated manufacturing using computer-aided design and other related fields [8–12]. One of these industries may be computer vision [13–23], which can develop in the Industry 4.0 and Industry 5.0 development paradigms [24–34].

The purpose of this work is to present the data on the application of developments concerning the use of CV methods in the example of non-hydrogenated and hydrogen-saturated WPs.

2. Literature Review and Some Theoretical Approaches

The operation of machines and mechanisms, for example, in power engineering, is accompanied by frictional contact of machine parts and mechanisms with hydrogen-containing process media, which significantly affects a number of alloy properties. The effect of H can be of a different nature. For example, at its low concentration, the alloy matrix material is ductile and has a predominantly viscous fracture character [35–42], and with an increase in its content and an increase in concentration in certain volumes, it can contribute to the "hydrogen embrittlement" of the matrix, i.e., the development and propagation of cracks [38,42–55], which can lead to catastrophic consequences during the operation of machine and mechanism components [46,56–63].

For the classical view of the behavior of a part under friction, we provide a diagram (Figure 1), which is supplemented with another diagram in the upper central part of the figure. According to this diagram, the following concept arises: as the concentration of hydrogen in the alloy increases, the influence of H on the probability of fracture of the part material increases.
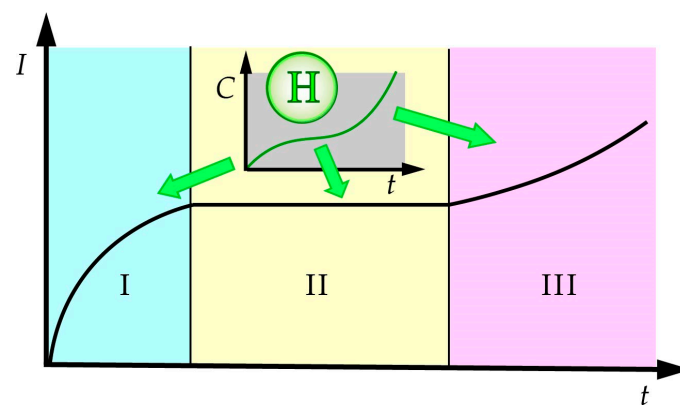

Figure 1. Conceptual diagram (scheme) (*I*—wear intensity; *C*—hydrogen concentration; *t*—time) of the effect of H (depending on its concentration in the alloy) on the wear resistance of a part under friction and long-term operation. Mode I—run-in; II—normal operation; III—catastrophic failure.

Thus, at a low H concentration in mode I, the effect of hydrogen is not significant; under normal operating conditions (mode II), it also has no significant effect on the destruction processes; and for mode III, an increase in the hydrogen concentration leads to catastrophic destruction of the part material and its failure. Each mode has its own morphology of wear particles and friction surfaces. For different steels and alloys, as well as wear conditions, the given ranges and shapes of the curves will be different.

A thorough study of the morphology of both the WPs and friction surfaces using CV methods can be automated, which will allow you to control the wear of the axes in the tribological connection and, therefore, prevent catastrophic destruction of the materials of the parts.

The identification of the morphology of friction surfaces is described in the following works [64–75], and some approaches and methods for identifying friction particles are described in [76–81]. In [76], the authors partially investigated granular materials (under some assumptions, steels can also be considered granular materials), which are widely used in nature and industry, and the discrete element method (DEM) is effective for their mechanical analysis. The determination of the friction coefficient remains a difficult task in DEM, so experiments were conducted to establish it between timbers of different shapes and boundaries. The results were approximated and integrated into DEM software

(https://altair.com/edem, accessed on 17 October 2024), after which additional experiments were performed. The analysis showed high consistency of the simulation results with the experimental data, which confirmed the theoretical validity of the methods and increased the accuracy of the DEM, and liding friction coefficients were determined by simulation and compared with experimental data. In [77], the sliding contact of third-body particles between rough rubber surfaces with waviness was experimentally investigated. The experiment isolated direct contact, where frictional resistance arose from the interaction of particles with rubber surfaces. In dry contact, the particles behaved like a clean roller, and the friction resistance did not depend on their size but varied depending on the position of the waviness. When lubricated, a particle would quickly roll down to the valley of the waviness and stop, waiting for a significant force to move. Lubrication increased the macroscopic friction resistance. An approximate solution for understanding the behavior of friction in dry contact was proposed.

Iron (Fe), the main component of brake wear particles, has different effects depending on the chemical compounds. Study [78] evaluated the contribution of oxides and hydroxides of iron to wear particles under real driving conditions with different friction materials of brake pads. Significant differences in wear resistance and PM10 and PM2.5 emissions were found between organic (NAO) and European (ECE) brake pads. Iron was the main particle component for both types of pads, but magnetite was less prevalent in NAO. This was indicative of ternary oxidation reactions in NAO. Differences in the phase transformations of iron and in the distribution of oxides and hydroxides between the materials were found.

For road and rail projects, the choice of aggregates depends on the characteristics of the local soil. In the design of geosynthetic-reinforced structures (GRSs), simple soil properties are often used without taking into account reinforcement. To study the effect of aggregates with different particle sizes on the friction between a geogrid and the soil, a large machine [79] was used for push-out testing. The tests showed that a larger particle size (gravel) provides more shear stress than smaller aggregates (sand, silt). Discrete element method (DEM) analysis indicated a greater interlocking effect between the geogrid and the soil for larger particles, resulting in a higher push-out force.

The authors of [80] noted that ships require oil for lubrication and energy transfer, which contain WPs. The identification of WP materials and sizes helps to understand wear. The existing online detection methods do not allow for simultaneous and continuous identification of materials and particle sizes. The paper proposed a neural network-based method for resolved tasks. The tree network model was trained step by step, and the accuracy of material and size identification reached 98% and 95%, respectively. The method showed high efficiency and robustness.

Paper [81] proposed a strategy for identifying the friction characteristic curve of a train wheel set under slippage based on a dynamic projection filter WP. The method used a multidimensional particle filter (MDIPF) for parameter correction, which integrated the correlation between WPs for a more accurate state transition. Next, a particle refinement method based on the dynamic projection domain (DPD) was applied, which dynamically adjusted the projection domain. Finally, a multi-level estimation was proposed for friction curve identification (FFCC). The strategy was proven to be effective, providing fast and accurate FFCC identification.

The main trends related to the development and implementation of computer vision include the following statements [82–92]:

- Deep Learning Applications;
- Event-based vision;
- Hybrid Image Retrieval Systems;
- Smart Cities and Industrial Applications;
- Medical Imaging and Extended Reality;
- Improved Learning Methods.

These trends illustrate how computer vision is becoming increasingly versatile and integrated into various fields, using advances in artificial intelligence and machine learning to solve complex problems in real-world situations.

3. Materials and Investigation Methodology

A flowchart (Figure 2) is proposed that describes an algorithm that allows for the use of computer vision methods for recognizing and analyzing WPs.
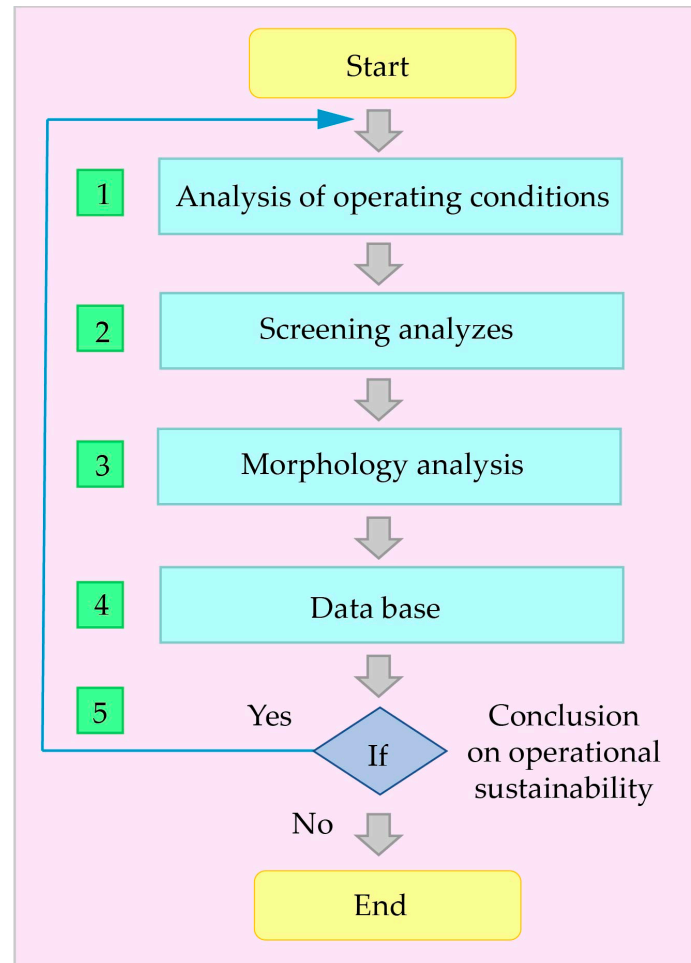

Figure 2. Conceptual flowchart of CV method applications for automatic WP analysis.

Stage 1 involves analyzing the operating conditions. Stage 2—conducting screening analyses—in this case, involves the selection of WPs. Stage 3 involves the analysis of WP morphology using computer vision methods. Stage 4 involves the analysis of the obtained results of use if there is already an existing database (classification of WPs according to their morphological characteristics) or the creation of a new database to compare the results obtained. Stage 5 involves drawing conclusions on the operational stability of the tribotechnical unit.

The materials of this work were digital photographs of steel WPs obtained with the help of microscopes. The system software was written in the Object Pascal programming language in the Delphi visual programming environment.

In our previous studies [93], we developed and worked out a methodology for determining the shape of the WP surface after dry and hydrogen wear by the CV system.

The following algorithm was used to obtain the shape of the WP surface. In the original image (Figure 3a), a region corresponding to the object under study (Figure 3b)

was selected. The high reflectivity of WPs compared to the background and threshold separation methods were used [94].
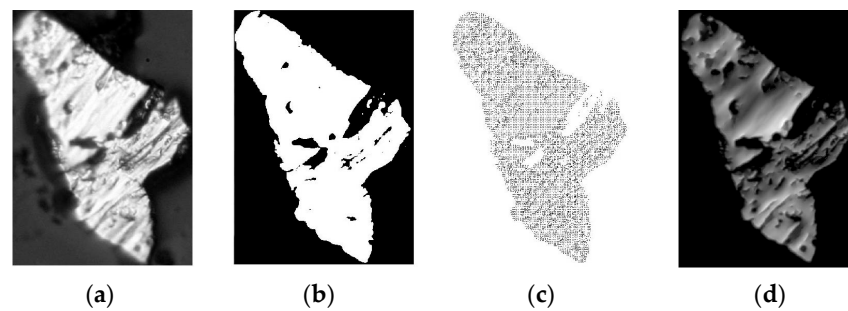

| (a) | (b) | (c) | (d) |

Figure 3. Stages of image processing: (**a**) original image, (**b**) binary image, (**c**) needle diagram, (**d**) range map [7].

The photograph of the part shown in Figure 3a was taken using a Neophot 2 microscope (Zeiss, Oberkochen, Germany) with a laptop and a Canon EOS 30D digital camera connected to it. The part shown in 3a was taken using a Neophot 2 microscope with a laptop and a Canon EOS 30D digital camera connected to it. This made it possible to determine the size of wear particles and photograph them in different lighting modes.

Then, the needle diagram of the object was calculated (Figure 3c), from which the range map was calculated (Figure 3d). The range map is presented in such a way that the lighter the pixel of the image, the closer the object surface is to the observer in this place. The range map contains information about the shape of the surface of the wear particle, which in this system is the output.

Next, we describe some of the mathematical apparatuses that were implemented in this methodology [7].

3.1. Range Map

Many different methods are used to describe the surface shape of recognized graphic objects [95]. In this work, the function $z(x, y)$ is used, given in the Cartesian rectangular coordinate system. Plane x, y coincides with the image plane and the axis, and the axis z is directed to the observer, as is customary in [96]. In a computer, the function $z(x, y)$ is presented in a discrete form. In this case, it is called a range map.

3.2. Needle Chart

When restoring the surface shape from a single halftone image, it is convenient to use the so-called needle diagram—the projection of unit normals to the object's surface onto the image plane. The direction of each normal is determined by only two parameters, $p = \partial z / \partial x$ and $q = \partial z / \partial y$, since these vectors have unit lengths [96]. If the range map is known $z(x, y)$, then it can be used to restore the needle chart—by finding the first partial derivatives p and q from this function. The inverse problem is unstable, but regularization methods can cope with this problem.

3.3. Reflectivity Map

To unambiguously solve the problem of determining the shape of an object's surface from its single halftone image, you need to have knowledge of the reflective properties of the surface and the position of the light source. This information is contained in the reflectivity map of an object [96]. A reflectance map is a unit-normalized function $R(p, q)$ that relates the brightness of a pixel in an image to the orientation of an object's elementary area corresponding to that pixel.

In photometry, a distinction is made between diffuse and specular reflections of light from different surfaces. Since wear particles are composed of metal, they reflect light in a ze-ring fashion. However, because the surfaces of the particles are not smooth, this is the

reflection of a huge number of "mirrors" whose orientations vary slightly. This reflection is called glossy. To describe the reflectivity of WPs in this paper, the following scattering indicator is used

$$R(\beta) = (\cos \beta)^n \tag{1}$$

where β is the angle between the direction of "pure" specular reflection from the elementary site of the object and the direction to the observer (axis z) and n is a positive integer. At indicator $n >> 1$ (1), the curve is strongly extended forward, which is a characteristic feature of glossy reflections. The parameter n is an indicator of this elongation.

Using the theorems of Euclidean geometry, we can obtain the formula

$$\cos \beta = 2 \cos \alpha \cdot \cos \theta - \cos \gamma \tag{2}$$

where α is the angle between the normal to the elementary site of the object and the direction to the illumination source, θ is the angle between the normal to the elementary site and the direction to the observer (axis z), and γ is the angle between the direction to the illumination source and the direction to the observer. The angles on the right-hand side of expression (2) can be expressed through the gradient of the function [96]:

$$\cos \alpha = \frac{1 + p_s p + q_s q}{\sqrt{1 + p^2 + q^2} \sqrt{1 + p_s^2 + q_s^2}} \quad \cos \theta = \frac{1}{\sqrt{1 + p^2 + q^2}} \quad \cos \gamma = \frac{1}{\sqrt{1 + p_s^2 + q_s^2}}$$

where is the α angle between the normal to the elementary area of the object and the direction to the illumination source, θ is the angle between the normal to the elementary area and the direction to the observer (axis z), and γ is the angle between the direction to the illumination source and the direction to the observer. The angles in the right part of expression (2) can be expressed through the function $z(x, y)$ gradient using the known formulas [96]: where p_s and q_s are parameters determining the direction to the illumination source.

3.4. Building a Needle Diagram

Coordinates of normals to the object surface for some pixels can be unambiguously reconstructed from the image. This applies to normals on the contour bounding the object, on surface continuity discontinuities, and on "highlights"—the brightest points on the object surface. On the contour and on continuity discontinuities, the normals lie in the plane x, y and are directed orthogonally to the contour or discontinuity line. Bliki correspond to bright spots on the image because here, the direction to the observer and the direction of mirror reflection coincide. The normals in these points, in accordance with Alhazen's law, lie in the plane defined by the directions to the illumination source and to the observer, and their position is symmetrical with respect to these directions.

The normals at the remaining points are determined using the numerical iterative method proposed in [97]:

$$f_{kl}^{n+1} = \overline{f}_{kl}^{n} + \lambda [E_{kl} - R_s(f_{kl}^n, g_{kl}^n)] \; \partial R_s / \partial f, \tag{3}$$

$$g_{kl}^{n+1} = \overline{g}_{kl}^{n} + \lambda [E_{kl} - R_s(f_{kl}^n, g_{kl}^n)] \; \partial R_s / \partial g, \tag{4}$$

where $f = \frac{2p}{1 + \sqrt{1 + p^2 + q^2}}$, $g = \frac{2q}{1 + \sqrt{1 + p^2 + q^2}}$—coordinates of the stereographic projection [96], E_{kl}—brightness of the pixel with coordinates k, l in the image; R_s—reflectivity map expressed in stereographic coordinates; n—iteration number, and $\overline{f}$, $\overline{g}$—local averages f and g, determined by the formulas:

$$\overline{f}_{kl} = (1/5) \cdot (f_{k+1, l} + f_{k, l+1} + f_{k-1, l} + f_{k, l-1}) + (1/20) \cdot (f_{k+1, l+1} + f_{k+1, l-1} + f_{k-1, l-1} + f_{k-1, l+1}),$$

$$\overline{g}_{kl} = (1/5) \cdot (g_{k+1, l} + g_{k, l+1} + g_{k-1, l} + g_{k, l-1}) + (1/20) \cdot (g_{k+1, l+1} + g_{k+1, l-1} + g_{k-1, l-1} + g_{k-1, l+1}).$$

3.5. Range Map Calculation

If we know the values of p and q, we can recover $z(x, y)$ by integration along arbitrary curves in the plane

$$z(x, y) = z(x_0, y_0) + \int_{(x_0, y_0)}^{(x, y)} (pdx + qdy).$$

However, p and q are recovered from noisy data. Therefore, the integral may depend on the choice of path. Since we have both, and p, and q, we have more information than necessary. This allows us to use an optimization method to find the surface that best fits non-ideal gradient estimates [96]. In this paper, the following iterative algorithm was used for this purpose:

$$z_{kl}^{n+1} = \bar{z}_{kl}^n - (1/2) \cdot (p_{k+1, l} - p_{k-1, l} + q_{k, l+1} - q_{k, l-1}), \tag{5}$$

where $\bar{z}_{kl} = (1/5) \cdot (z_{k+1, l} + z_{k, l+1} + z_{k-1, l} + z_{k, l-1}) + (1/20) \cdot (z_{k+1, l+1} + z_{k+1, l-1} + z_{k-1, l-1} + z_{k-1, l+1})$.

Based on the above data, we have developed a computer program [98] that allows us to conduct precedent-setting studies of destroyed surfaces.

The photographs of the particles shown in Figure 4 were taken on a modern Zeiss EVO-40XVP electron microscope (Oberkochen, Germany) with INCA Energy and AZtec HKL Advanced energy dispersive microanalysis and backscattered electron diffraction systems based on a Nordlys Nano detector from Oxford Instruments.
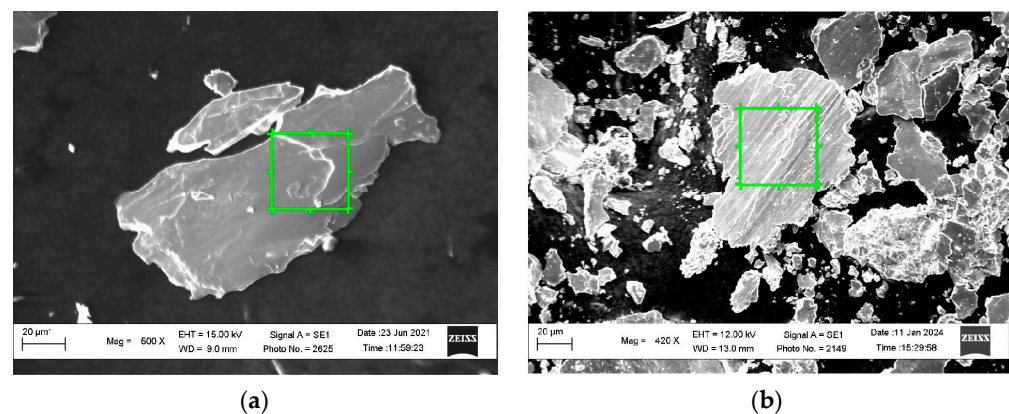

(**a**)   (**b**)

Figure 4. Photograph of wear particles formed under dry friction conditions (p = 250 N): without flooding (**a**) and after electrolytic flooding (**b**). The green color outlines the square whose area was studied using a computer vision system.

4. Results and Discussions

The developed CP was used to study the wear particles of high-nitrogen steel before and after flooding (Figure 4). High-nitrogen steels have a whole range of properties that allow them to be used in various fields, including as tribotechnical materials [99–110].

Figures 5 and 6 show the results of our own research to determine the features of the WP morphology in the form of print screens of dialog boxes with the CP.

Among the data calculated by the program, we highlight VERTEX, CAVITY, Nmax, and ENTROPY [111].

We obtained several dozen high-quality photographs of wear particles taken under various conditions, which can be used to expand the research horizons using computer vision methods to obtain various correlations.

We can also expand the possibilities of wear particle research by writing additional scripts, for example, in the Python language.
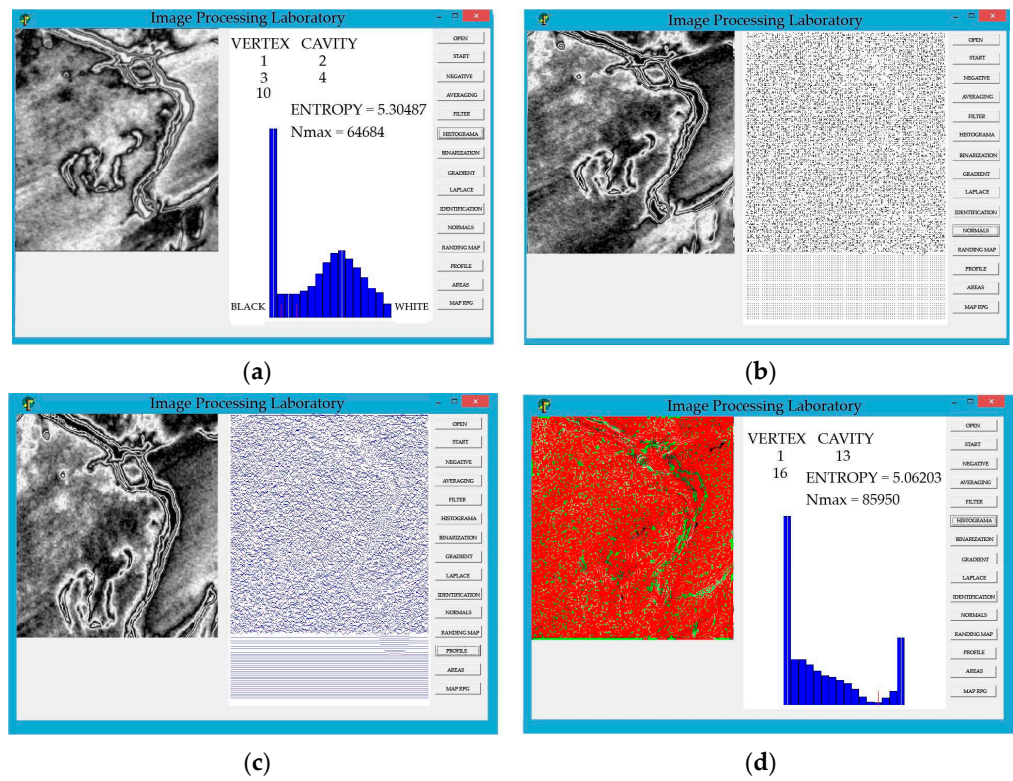
Figure 5. Examination of digital images of non-flooded WPs using the developed CP: histogram construction operation (**a**), the operation of constructing normals (**b**), creating a surface profile (**c**), calculation of the surface profile with the construction of histograms (**d**).
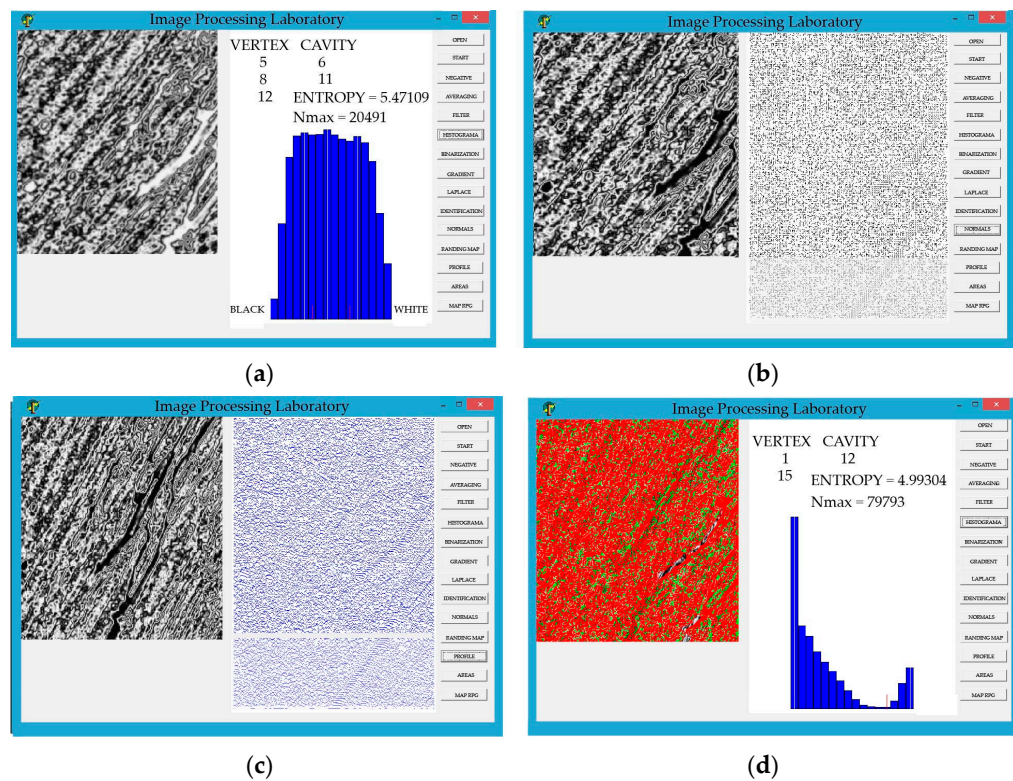

Figure 6. Examination of digital images of the flooded WPs using the developed CP: histogram construction operation (**a**), the operation of constructing normals (**b**), creating a surface profile (**c**), calculation of the surface profile with the construction of histograms (**d**).

Figure 7a,b show a photograph of the image that was prepared for further research. Figure 7c,d show an image that was generated as a binary image.
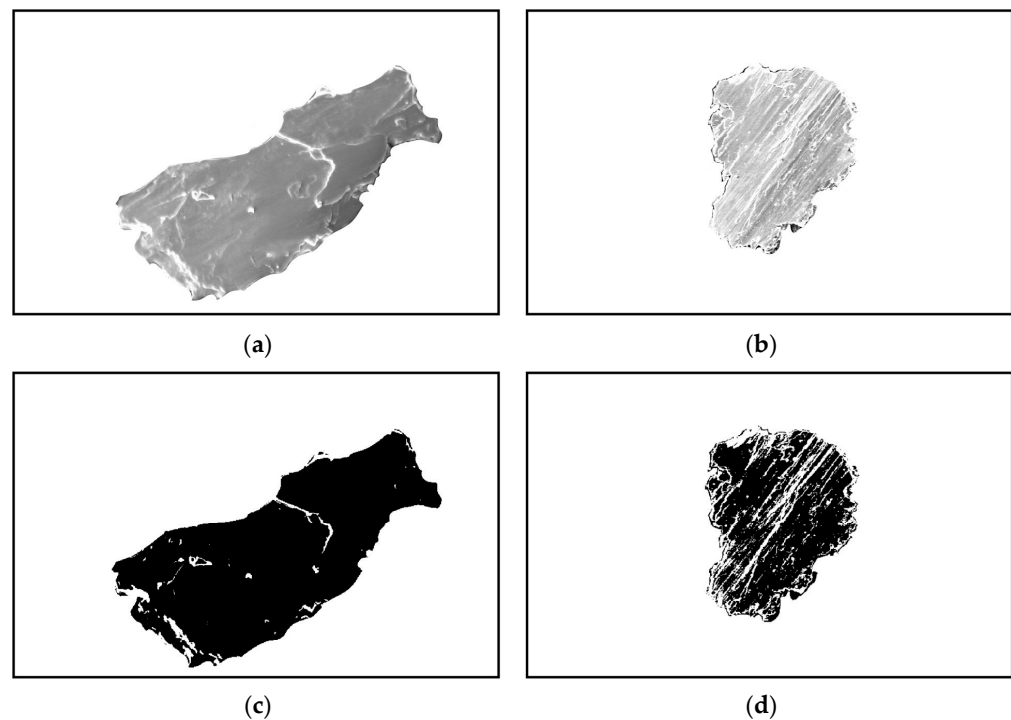

(**a**)

(**b**)

(**c**)

(**d**)

Figure 7. Images of wear particles prepared for computer vision processing. Non-hydrogen changing particle (**a**,**c**). Hydrogen changing particle (**b**,**d**). Binary image (**c**,**d**).

Appendix A provides the computer code that was used to carry out the following studies with wear particles.

This code was used to perform the following:

1. Load two gray-scale images.
2. Binarize the image based on the average luminance value.
3. Mark regions in the image and calculate their properties.
4. Display the binarized image.
5. Convert the results into a table for easy viewing.

Particle shape analysis was performed on both images. For each particle, parameters such as area, perimeter, eccentricity, and density were calculated. The data obtained from the tabular form are presented in the form of graphs (Figures 8–11).

Here, we provide a description of each chart (Figures 8–11). First, we describe the comparison of area (Figure 8).

This graph shows the area of each particle for two images. Area defines the number of pixels that make up a particle. You can see how particle size varies between the two images, including which particles are larger or smaller in area.

Next, we describe the perimeter comparison of the area (Figure 9).

The graph shows the length of the perimeter of each particle in both images. The perimeter measures the number of pixels that form the outline of the particle. This helps you understand how complex or irregular the particle shapes are.

Next, we describe the comparison of eccentricity (Figure 10).

The eccentricity reflects the degree to which a particle's shape deviates from a perfect circle. A value close to 0 indicates a particle that is more like a circle, and a value close to 1 indicates an elongated or linear particle. This graph helps to understand the shape of the particles and their orientation.

Finally, we describe the comparison of solidity (Figure 11).

Density is defined as the ratio of the area of a particle to the area of its convex hull. A value closer to 1 indicates that the particle has a simple, compact shape, while a lower value indicates a complex, branched shape. This graph illustrates how compact the particles in each image are.
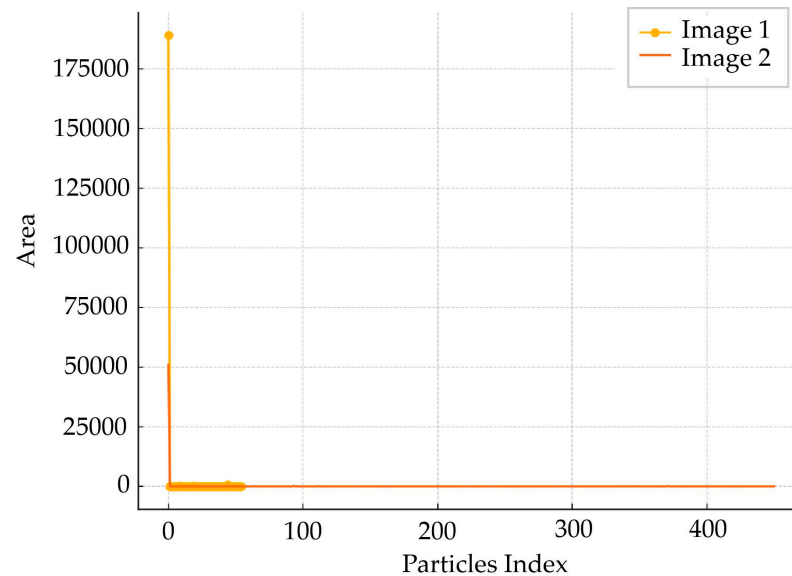

Figure 8. Comparison of area. Image 1—non-hydrogen charging. Image 2—hydrogen charging.
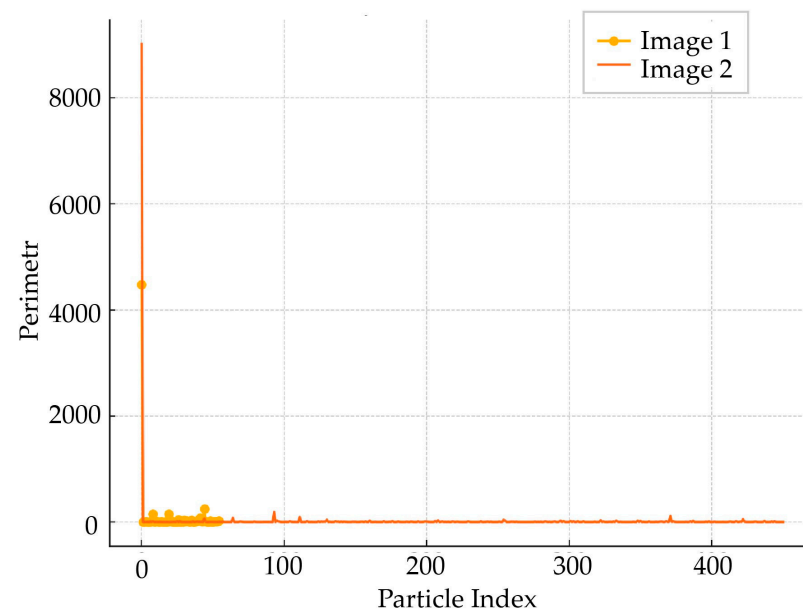

Figure 9. Comparison of perimeter. Image 1—non-hydrogen charging. Image 2—hydrogen charging.

Next, we describe some additional computer vision studies that can be performed with the above wear particles.

Shape and distribution analysis:

- *Classify particles by shape:*

Use clustering (e.g., k-means) to group particles based on their characteristics (area, perimeter, eccentricity, density).

- *Particle size distribution.*

Create histograms to analyze the distribution of areas or perimeters.

- *Estimation of anisotropy.*

Analyze the direction of elongation of particles to study the dominant orientation in the material.

Detecting defects:

- *Search for cracks or voids.*

Use edge detectors (Sobel, Canny) to identify areas that indicate defects or microcracks.

- *Estimation of defect density.*

Count the number of defects per unit area or estimate their effect on the shape of the particle.

Texture analysis:

- *Texture features (GLCM, LBP).*

Use texture analysis techniques (e.g., gray-level correlation matrix, local binary patterns) to determine the internal structure of particles.

- *Texture classification.*

Apply machine learning to classify particles based on texture features (e.g., smooth, rough, cracked).

Three-dimensional modeling:

Reconstruction of 3D models.

- If image series are available, a 3D particle model can be reconstructed to analyze volume, shape, and structure.

Damage simulation.

- Simulate the effect of cracks on particle shape in three dimensions.

Dynamic analysis:

- *Tracking the movement of particles.*

If a series of images are available over time, the movement of particles can be tracked to analyze their interactions.

- *Fragmentation studies.*

Analyze how large particles are divided into smaller ones under load.

Comparison with samples:

- *Comparison with reference data.*

Use reference particles or samples to assess whether the particles being analyzed meet certain standards (e.g., size, shape, defects).

- *Estimate the level of wear.*

Compare particles from different samples to estimate the degree of wear.

Semantic segmentation:

- *Separation into regions of interest.*

Use semantic segmentation techniques (e.g., U-Net neural networks) to separate particles from the background or to highlight defects.

- *Analysis of complex structures.*

Segment areas of high and low material density.

Integration with machine learning:

- *Automatic classification.*

Use machine learning algorithms to automatically classify particles according to their characteristics (e.g., healthy/defective).

- *Prediction of material properties.*

Use particle shape data to predict physical and mechanical properties.

Modeling of interaction with hydrogen:

- *Analysis of the impact of hydrogen.*

Model which particles are more vulnerable to hydrogen exposure based on their area, density, and shape.

- *Visualization of hydrogen concentration.*

Integrate fluorescence analysis data to create heat maps of hydrogen distribution on particles. These studies can help to deepen the understanding of material characteristics and assess how various factors affect particle properties.

Concept for the Construction and Implementation of a Scheme for Determining the Performance and Technical Condition of a Tribotechnical Unit

To implement the above data in the "industry" on the basis of the above algorithm (Figure 2), we propose the following scheme (Figure 12). To use it, it is first necessary to select WPs (screening analysis) and to study WPs by CV methods with the identification of the most typical ones that correspond to the four main operating modes (Figure 7). We calculate two parameters: the index of performance modes and operational status (IOPMAOS) scale size from 0 to 10 and the integral defect criterion based on screening analyses (IDCBOSA) scale size from 0 to 12.

This technique can be used not only for WPs but also for chips, friction surfaces, cutting surfaces, and technological surfaces of complex alloy steels and alloys containing cracks, damage, and changes in the micro-rail during the entire life cycle of the part and tribotechnical assembly [112–128].

Further development of CV methods and computer modeling [129–139] will expand the horizons of the application of the above technologies.
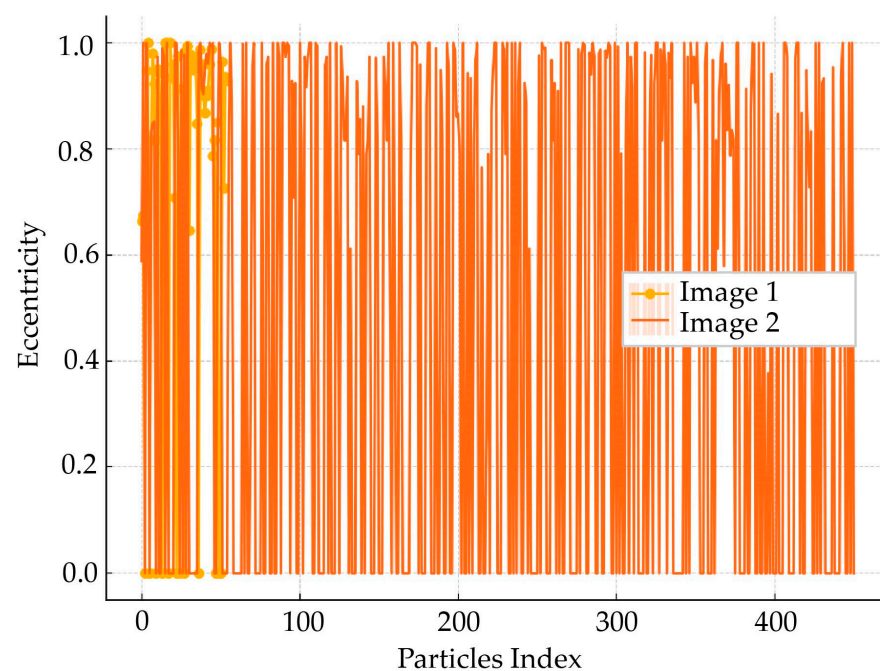

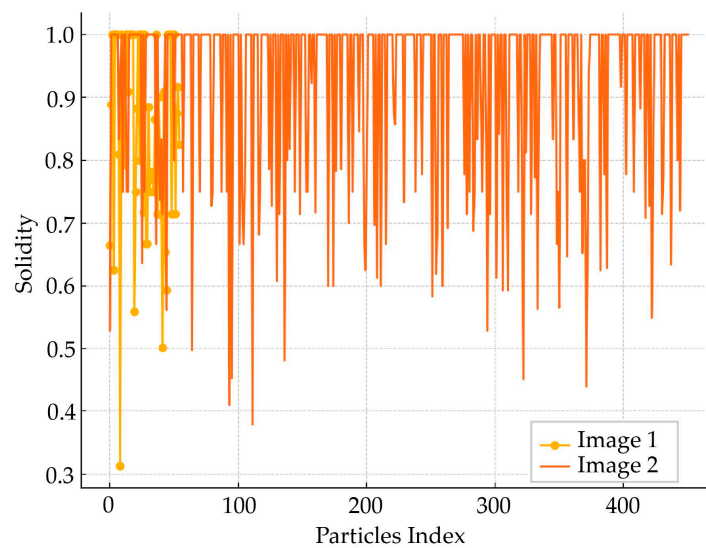**Figure 10.** Comparison of eccentricity. Image 1—non-hydrogen charging. Image 2—hydrogen charging.

Figure 11. Comparison of solidity. Image 1—non-hydrogen charging. Image 2—hydrogen charging.
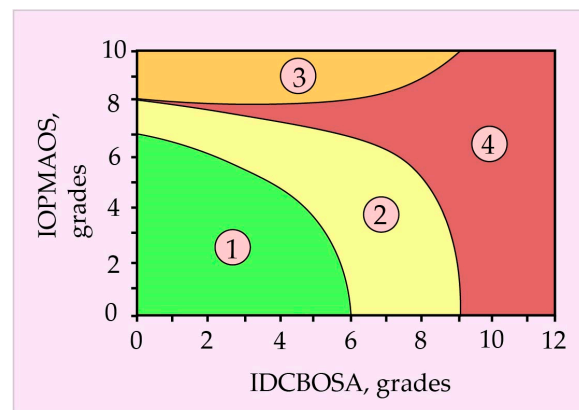

Figure 12. Conceptual scheme for determining the performance of a tribotechnical assembly depending on the determined WP parameters. Designation of modes: 1—normal operation; 2—transient; 3—running-in; 4—catastrophic failure.

Deep learning and image segmentation are key areas in computer vision. One of the most popular models for segmentation is U-Net and its variations Mask R-CNN and YOLO [140–144].

Study [145] explored automated fracture identification in material testing using deep learning convolutional neural networks (CNNs). Three experiments—uniaxial tensile, punch, and shear—were analyzed. Transfer learning was employed with VGG, ResNet, and Inception CNN architectures. Moderate-sized filters and deeper architectures yielded validation accuracies exceeding 95%. Low-cost models optimized for minimal storage and computing power also achieved high performance. Greedy network searches identified architectures exceeding 99% validation accuracy, eliminating low-performing counterparts. CNN-based "all-in-one" fracture models were developed for automated, computer vision-driven characterization. Feature map analysis highlighted the networks' capability for salient feature detection. Automated crack localization and profiling were demonstrated using LIME and image subset creation. The findings established a foundation for automating material testing with reliable deep learning methods. These techniques aim to streamline labor-intensive engineering tasks and enhance analysis reliability.

Periodic fractographic analysis [146] improves the performance of mechanical components and prevents economic and security issues, especially in industries like automotive. Classifying fractures by failure modes is crucial to identifying their root causes. Experts

rely on visual evidence, such as textures and surface marks, to classify metallic material fractures. The cited study used two datasets: a real-scale fracture dataset and SEM images at various scales. Fracture classification performance was evaluated using traditional convolutional neural networks for object and texture analysis. A deep learning architecture incorporating adaptive wavelet transform for textural feature extraction was also introduced. The experimental results confirmed the effectiveness of deep learning in extracting textural features. These methods significantly enhanced mechanical failure classification. The findings demonstrated the potential of advanced techniques for accurate fracture analysis. This approach supports improved reliability in mechanical systems.

Fracture surface analysis [147] is crucial for ensuring the structural integrity of metallic materials, especially additively manufactured ones. Despite advancements in testing automation, fatigue fracture image analysis is often performed manually by experts. This approach, while accurate, requires extensive expertise and has limitations. The cited study presented an unsupervised tool to assist non-experts in identifying fracture origins. Developed using fatigue fracture image specimens, the tool focuses on detecting river marks. It accommodates various recording parameters if preprocessing settings are adjusted. The tool can analyze other materials with river-marked fracture surfaces. However, cases with multiple origins or origins near the surface require further tool development. This method reduces reliance on expert knowledge while improving analysis efficiency. It also highlights the need for continued refinement to address complex fracture scenarios.

Also relevant is the work of [148], which utilized an automated system to classify fatigue, abrasive, and adhesive wear particles. Fatigue particles were generated using an FZG gear test rig, while a pin-on-disk tribometer produced abrasive and adhesive particles. SEM images of wear particles were collected to form a database for analysis. Particles were grouped into three classes, each representing a distinct wear mechanism. Visual examination was conducted for each class, followed by the calculation of parameters like area, perimeter, convexity, and elongation using image analysis software. Statistical analysis was performed on these parameters. The automated system then classified particles based on surface texture. The results were compared with visual assessments and numerical parameter evaluations. The texture-based system proved more efficient and accurate than size- and shape-based methods. This approach shows great potential for enhancing machine condition monitoring. Its accuracy and efficiency make it a promising tool for distinguishing wear mechanisms. The method can significantly improve industrial monitoring processes.

Study [149] proposed an algorithm that combines ResNet50 and the Separable Vision Transformer (SepViT) to tackle challenges such as complex backgrounds, overlapping features, and low accuracy in classifying small wear particles. Using ESRGAN for image resolution enhancement, the SV-ERnet model integrates ResNet50 and SepViT via weighted soft voting and applies transfer learning for intelligent particle identification. Grad-CAM visualization reveals the model's focus on different abrasive characteristics. Achieving 94.1% accuracy on the test set, it outperformed ResNet101, VGG16, MobileNetV2, AlexNet, and EfficientV1 by margins of 1.8% to 6.8%. Optimal weighting factors were determined to be 0.5 for both components.

An enhanced YOLOv8 algorithm [150] addresses challenges in detecting complex, overlapping, and small wear particles in ferrographic images. Improvements include integrating Deformable Convolutional Network v3 for better feature extraction, using the Dysample method for clearer upsampling, and optimizing the detection head for faster convergence and higher precision. This approach achieves a 5.6% increase in average precision without compromising detection speed (111.6 FPS), supporting online monitoring applications.

The proposed EYBNet ferrography [151] detection network addresses false and missed detection of small, dense, and overlapping wear particles in complex oil backgrounds. It uses the MSRCR algorithm to enhance image contrast and reduce background interference, improves YOLOv5s accuracy with DWConv and optimized loss functions, and adds ECAM for better feature expression. The path aggregation network is replaced with a weighted

BiFPN for efficient cross-scale connections. EYBNet achieves a 4.46% increase in accuracy (91.3%) and a detection speed of 50.5 FPS, outperforming YOLOv5s.

The role of a person in the Industry 5.0 paradigm in the interaction with wear products of hydrogen-saturated steels is that a person acts as an operator who corrects and analyzes the data obtained with the help of microscopes. A person has scientific experience, as well as a set of skills such as "observation", which allows for preparing reliable and validated data for robotic systems from the first human person. This has not yet been analyzed and processed with the help of computer programs.

5. Conclusions

- A conceptual scheme is proposed to illustrate how the hydrogen concentration affects the wear resistance of materials during friction and long-term operation. Three modes are identified, including running-in, normal operation, and catastrophic failure, each with distinct wear particle morphologies. Low hydrogen concentrations enhance plasticity, while high levels cause embrittlement and catastrophic failure.
- Key trends in computer vision (CV) development are outlined, including deep learning, event-based vision, hybrid retrieval systems, smart applications, medical imaging, and improved learning techniques.
- A flowchart for CV-based wear particle analysis is presented. It includes steps such as analyzing operating conditions, conducting screening, assessing particle morphology, comparing results with a database, and determining operational stability.
- A CV system and mathematical methods are used to analyze wear particle shapes after dry and wet wear. Techniques such as high reflectivity detection and threshold separation are applied.
- An example study on high-nitrogen steel wear particles before and after flooding demonstrates software capabilities, including calculations for VERTEX, CAVITY, Nmax, and ENTROPY, describing surface morphology.
- We propose to continue scientific research on wear particles. The main paradigm is the use of the Python programming language. As for further research, the following can be distinguished: 1. Shape and distribution analysis. 2. Detecting defects. 3. Texture analysis. 4. Three-dimensional modeling. 5. Dynamic analysis. 6. Comparison with samples. 7. Semantic segmentation. 8. Integration with machine learning. 9. Modeling of the interaction with hydrogen.
- A framework for evaluating tribotechnical unit performance is proposed, using wear particle analysis and key metrics like the performance mode index and defect criteria.
- The CV methodology for analyzing wear particle surfaces is applicable to friction surfaces, corrosion products, and chips from manufacturing and repair processes, broadening its usability.

Conflicts of Interest: The authors declare no personal circumstances or interests that may be perceived as inappropriately influencing the representation or interpretation of the reported research results.

Nomenclature and Abbreviations

CV — computer vision
WPs — wear particles
CP — computer program
H — hydrogen
GLCM — Gray-Level Co-occurrence Matrix;
LBPs — local binary patterns

Appendix A

```python
from skimage import io, measure
import matplotlib.pyplot as plt
import pandas as pd

# Uploading images
image_path_1 = '/mnt/data/01.png'
image_path_2 = '/mnt/data/02.png'

image_1 = io.imread(image_path_1, as_gray=True)
image_2 = io.imread(image_path_2, as_gray=True)

# Image analysis function
def analyze_image(image, title):
    # Image binarization (simple threshold)
    binary_image = image > image.mean()

    # Labeling binary images
    labeled_image = measure.label(binary_image)

    # Derivation of properties of markovaniye regions
    properties = measure.regionprops_table(
        labeled_image,
        properties=('area', 'perimeter', 'eccentricity', 'solidity')
    )

    # Displaying a binary image
    plt.figure(figsize=(8, 6))
    plt.imshow(binary_image, cmap='gray')
    plt.title(f'Binary Image: {title}')
    plt.axis('off')
    plt.show()

    return properties

# Analyzing the first image
properties_1 = analyze_image(image_1, "Image 1")
properties_2 = analyze_image(image_2, "Image 2")

# Convert results to a DataFrame for visualization
df_1 = pd.DataFrame(properties_1)
df_2 = pd.DataFrame(properties_2)

# Displaying the results
import ace_tools as tools
tools.display_dataframe_to_user(name="Analysis of Image 1", dataframe=df_1)
```

tools.display_dataframe_to_user(name="Analysis of Image 2", dataframe=df_2)

References

1. Balyts'kyi, O.I.; Kolesnikov, V.O. Investigation of wear products of high-nitrogen manganese steels. *Mater. Sci.* **2009**, *45*, 576–581. [CrossRef]
2. Balyts'kyi, O.I.; Kolesnikov, V.O. Investigation of the wear products of austenitic manganese cast irons. *Mater. Sci.* **2004**, *40*, 78–82. [CrossRef]
3. Balyts'Kyi, O.I.; Kolesnikov, V.O.; Eliasz, J. Study of the wear resistance of high-nitrogen steels under dry sliding friction. *Mater. Sci.* **2013**, *48*, 642–646. [CrossRef]
4. Balitskii, O.A.; Kolesnikov, V.O.; Balitskii, A.I. Wear resistance of hydrogenated high nitrogen steel at dry and solid state lubricants assist ant friction. *Arch. Mater. Sci. Eng.* **2019**, *98*, 57–67. [CrossRef]
5. Balyts'kyi, O.I.; Kolesnikov, V.O.; Eliasz, Y.; Havrylyuk, M.R. Specific features of the fracture of hydrogenated high-nitrogen manganese steels under conditions of rolling friction. *Mater. Sci.* **2015**, *50*, 604–611. [CrossRef]
6. Balitskii, A.I.; Syrotyuk, A.M.; Ivaskevich, L.M.; Balitskii, O.A.; Kochmanski, P.; Kolesnikov, V.O. Hydrogen accelerated nanopore nucleation, crack initiation and propagation in the Ni–Co superalloys. *Int. J. Hydrogen Energy* **2024**, *82*, 320–332. [CrossRef]
7. Balitskii, O.; Kolesnikov, V. Identification of wear products in the automotive tribotechnical system using computer vision methods, artificial intelligence and Big Data. In Proceedings of the 2019 XIth International Scientific and Practical Conference on Electronics and Information Technologies (ELIT), Lviv, Ukraine, 16–18 September 2019; IEEE: Piscataway, NJ, USA, 2019; pp. 24–27. [CrossRef]
8. Quintana, J.J.; Ferrer, M.A.; Diaz, M.; Feo, J.J.; Wolniakowski, A.; Miatliuk, K. Uniform vs. Lognormal Kinematics in Robots: Perceptual Preferences for Robotic Movements. *Appl. Sci.* **2022**, *12*, 12045. [CrossRef]
9. Schlette, C.; Buch, A.G.; Hagelskjær, F.; Iturrate, I.; Kraft, D.; Kramberger, A.; Thulesen, T.N. Towards robot cell matrices for agile production—SDU Robotics' assembly cell at the WRC. *Adv. Robot.* **2018**, *34*, 422–438. [CrossRef]
10. Wolniakowski, A.; Trochimczuk, R.; Moulianitis, V.; Miatliuk, K. Kinematic Modeling of a Trepanation Surgical Robot System. *Appl. Sci.* **2023**, *13*, 9110. [CrossRef]
11. Ellekilde, L.-P.; Wilm, J.; Nielsen, O.W.; Krogh, C.; Kristiansen, E.; Gunnarsson, G.G.; Stenvang, J.; Jakobsen, J.; Kristiansen, M.; Glud, J.A.; et al. Design of Automated Robotic System for Draping Prepreg Composite Fabrics. *Robotica* **2021**, *39*, 72–87. [CrossRef]
12. Valsamos, C.; Miatliuk, K.; Wolniakowski, A.; Moulianitis, V.; Aspragathos, N. Optimal Kinematic Task Position Determination—Application and Experimental Verification for the UR-5 Manipulator. *Appl. Sci.* **2022**, *12*, 9352. [CrossRef]
13. Cejnek, M.; Oswald, C. Machine vision object measurement in difficult industry environment. *Proceedings* **2019**, *37*, 26. [CrossRef]
14. Buch, A.G.; Petersen, H.G.; Krüger, N. Local shape feature fusion for improved matching, pose estimation and 3D object recognition. *SpringerPlus* **2016**, *5*, 294. [CrossRef] [PubMed]
15. Cardoso, B.; Silva, C.; Costa, J.; Ribeiro, B. Internet of Things Meets Computer Vision to Make an Intelligent Pest Monitoring Network. *Appl. Sci.* **2022**, *12*, 9397. [CrossRef]
16. Fan, X.; Liu, T.; Bao, H.; Pan, W.; Liang, T.; Li, H. Long-Tail Instance Segmentation Based on Memory Bank and Confidence Calibration. *Appl. Sci.* **2022**, *12*, 9366. [CrossRef]
17. Strelkova, T.A.; Lytyuga, A.P.; Kalmykov, A.S. Statistical characteristics of optical signals and images in machine vision sys-tems. In *Examining Optoelectronics in Machine Vision and Applications in Industry 4.0*; IGI Global: Hershey, PA, USA, 2021; pp. 134–162. [CrossRef]
18. Javaid, M.; Haleem, A.; Singh, R.P.; Rab, S.; Suman, R. Exploring impact and features of machine vision for progressive Indus-try 4.0 culture. *Sensors* **2022**, *3*, 100132. [CrossRef]
19. Miranda-Vega, J.E.; Rivera-Castillo, J.; Rivas-López, M.; Flores-Fuentes, W.; Sergiyenko, O.; Rodríguez-Quiñonez, J.C.; Hernández-Balbuena, D. Reducing the optical noise of machine vision optical scanners for landslide monitoring. In *Examining Op-toelectronics in Machine Vision and Applications in Industry 4.0.*; IGI Global: Hershey, PA, USA, 2021; pp. 103–133. [CrossRef]
20. Silva, R.L.; Rudek, M.; Szejka, A.L.; Junior, O.C. Machine vision systems for industrial quality control inspections. In Proceedings of the IFIP International Conference on Product Lifecycle Management, Turin, Italy, 2–4 July 2018; Springer: Cham, Switzerland, 2018; pp. 631–641. [CrossRef]
21. Li, L.; Qiu, J.; Spratling, M. AROID: Improving Adversarial Robustness Through Online Instance-Wise Data Augmentation. *Int. J. Comput. Vis.* **2024**, 1–22. [CrossRef]
22. Graf, B.; Eckstein, J. Service Robots and Automation for the Disabled and Nursing Home Care. In *Springer Handbook of Automation. Springer Handbooks*; Nof, S.Y., Ed.; Springer: Cham, Switzerland, 2023; pp. 1331–1347. [CrossRef]
23. Ryan, E.; Roshandelpoor, A.; Pollard, Z.; Goldfarb, J.L.; Vakili, P. Prospective on methods of design of experiments for limited data scenarios in materials design and engineering. *MRS Commun.* **2023**, *13*, 1087–1101. [CrossRef]
24. Zou, L.; Cheng, H. Research on Wind Turbine Blade Surface Damage Identification Based on Improved Convolution Neural Network. *Appl. Sci.* **2022**, *12*, 9338. [CrossRef]
25. Adeyeri, M.K.; Mpofu, K.; Olukorede, T.A. Integration of agent technology into manufacturing enterprise: A review and platform for Industry 4.0. In Proceedings of the 2015 International Conference on Industrial Engineering and Operations Management (IEOM), Dubai, United Arab Emirates, 3–5 March 2015; IEEE: Piscataway, NJ, USA, 2015; pp. 1–10. [CrossRef]

26. Rai, R.; Tiwari, M.K.; Ivanov, D.; Dolgui, A. Machine learning in manufacturing and industry 4.0 Applications. *Int. J. Prod. Res.* **2021**, *59*, 4773–4778. [CrossRef]

27. Varshney, A.; Garg, N.; Nagla, K.S.; Nair, T.S.; Jaiswal, S.K.; Yadav, S.; Aswal, D.K. Challenges in sensors technology for industry 4.0 for futuristic metrological applications. *MAPAN* **2021**, *36*, 215–226. [CrossRef]

28. Moreno, A.; Velez, G.; Ardanza, A.; Barandiaran, I.; de Infante, Á.R.; Chopitea, R. Virtualisation process of a sheet metal punching machine within the Industry 4.0 Vision. *Int. J. Interact. Des. Manuf.* **2017**, *11*, 365–373. [CrossRef]

29. Oztemel, E.; Gursev, S. Literature review of Industry 4.0 and related technologies. *J. Intell. Manuf.* **2020**, *31*, 127–182. [CrossRef]

30. Barata, J.; Kayser, I. Industry 5.0—Past, Present, and Near Future. *Procedia Comput. Sci.* **2023**, *219*, 778–788. [CrossRef]

31. Ghobakhloo, M.; Iranmanesh, M.; Tseng, M.L.; Grybauskas, A.; Stefanini, A.; Amran, A. Behind the definition of Industry 5.0: A systematic review of technologies, principles, components, and values. *J. Ind. Prod. Eng.* **2023**, *40*, 432–447. [CrossRef]

32. Tzampazaki, M.; Zografos, C.; Vrochidou, E.; Papakostas, G.A. Machine Vision—Moving from Industry 4.0 to Industry 5.0. *Appl. Sci.* **2024**, *14*, 1471. [CrossRef]

33. Valette, E.; El-Haouzi, H.B.; Demesure, G. Industry 5.0 and its technologies: A systematic literature review upon the human place into IoT- and CPS-based industrial systems. *Comput. Ind. Eng.* **2023**, *184*, 109426. [CrossRef]

34. Demir, K.A.; Döven, G.; Sezen, B. Industry 5.0 and Human-Robot Co-Working. *Procedia Comput. Sci.* **2019**, *158*, 688–695. [CrossRef]

35. Takazaki, D.; Tsuchiyama, T.; Komoda, R.; Dadfarnia, M.; Somerday, B.P.; Sofronis, P.; Kubota, M. Effect of Hydrogen on Creep Properties of SUS304 Austenitic Stainless Steel. *Corrosion* **2021**, *77*, 256–265. [CrossRef]

36. Ogawa, Y.; Hosoi, H.; Tsuzaki, K.; Redarce, T.; Takakuwa, O.; Matsunaga, H. Hydrogen, as an alloying element, enables a greater strength-ductility balance in an Fe-Cr-Ni-based, stable austenitic stainless steel. *Acta Mater.* **2020**, *199*, 181–192. [CrossRef]

37. Mytsyk, B.; Ivanytsky, Y.; Hembara, O.; Kost, Y.; Shtayura, S.; Sakharuk, O. Effects of hydrogen influence on strained steel 1020. *Int. J. Hydrogen Energy* **2020**, *45*, 10199–10208. [CrossRef]

38. Dmytrakh, I.M.; Leshchak, R.L.; Syrotyuk, A.M.; Barna, R.A. Effect of hydrogen concentration on fatigue crack growth behaviour in pipeline steel. *Int. J. Hydrogen Energy* **2017**, *42*, 6401–6408. [CrossRef]

39. Rao, G.S.; Seifert, H.-P.; Ritter, S.; Spätig, P.; Que, Z. Effect of hydrogen on tensile behavior of low alloy steel in the regime of dynamic strain ageing. *Procedia Struct. Integr.* **2016**, *2*, 3399–3406. [CrossRef]

40. Sun, Y.; Chen, J.; Liu, J. Effect of hydrogen on ductility of high strength quenched and tempered (QT) Cr–Ni–Mo steels. *Mater. Sci. Eng. A* **2015**, *625*, 89–97. [CrossRef]

41. Liu, Y.; Wang, M.; Liu, G. Effect of hydrogen on ductility of high strength 3Ni–Cr–Mo–V steels. *Mater. Sci. Eng. A* **2014**, *594*, 40–47. [CrossRef]

42. Ostash, O.P.; Vytvyts'kyi, V.I. Duality of the action of hydrogen on the mechanical behavior of steels and structural optimization of their hydrogen resistance. *Mater Sci.* **2012**, *47*, 421–437. [CrossRef]

43. Khatib Zadeh Davani, R.; Mohtadi-Bonab, M.A.; Yadav, S.; Entezari, E.; Cabezas, J.F.A.; Szpunar, J. Effect of Quench Tempering on Hydrogen Embrittlement and Corrosion Behavior of X100 Pipeline Steel. *Metals* **2023**, *13*, 841. [CrossRef]

44. Martin, M.L.; Connolly, M.J.; DelRio, F.W.; Slifka, A.J. Hydrogen embrittlement in ferritic steels. *Appl. Phys. Rev.* **2020**, *7*, 12851. [CrossRef]

45. Fan, Y.; Ma, C.; Li, S.; Ding, W.; Zhang, H. A review on the effect of microstructure on hydrogen induced cracking behaviour in pipeline and pressure vessel steels. In Proceedings of the 2020 6th International Forum on Engineering Materials and Manufacturing Technology (IFEMMT) 2020, Jilin, China, 17–19 July 2020; IOP Publishing: Bristol, UK, 2020. Available online: https://iopscience.iop.org/article/10.1088/1742-6596/1635/1/012055 (accessed on 17 October 2024).

46. Sobola, D.; Dallaev, R. Exploring Hydrogen Embrittlement: Mechanisms, Consequences, and Advances in Metal Science. *Energies* **2024**, *17*, 2972. [CrossRef]

47. Barrera, O.; Bombac, D.; Chen, Y.; Daff, T.D.; Galindo-Nava, E.; Gong, P.; Haley, D.; Horton, R.; Katzarov, I.; Kermode, J.R.; et al. Understanding and mitigating hydrogen embrittlement of steels: A review of experimental, modelling and design progress from atomistic to continuum. *J. Mater. Sci.* **2018**, *53*, 6251–6290. [CrossRef]

48. Mohtadi-Bonab, M.A.; Szpunar, J.A.; Basu, R.; Eskandari, M. The mechanism of failure by hydrogen induced cracking in an acidic environment for API 5L X70 pipeline steel. *Int. J. Hydrogen Energy* **2015**, *40*, 1096–1107. [CrossRef]

49. Dmytrakh, I.M.; Leshchak, R.L.; Syrotyuk, A.M. Effect of hydrogen concentration on strain behaviour of pipeline steel. *Int. J. Hydrogen Energy* **2015**, *40*, 4011–4018. [CrossRef]

50. Bae, K.O.; Nguyen, T.T.; Park, J.; Park, J.S.; Baek, U.B. Temperature dependency of hydrogen-related impact energy degradation of type 304 austenitic stainless steel. *J. Mech. Sci. Technol.* **2023**, *37*, 2891–2901. [CrossRef]

51. Pradhan, A.; Vishwakarma, M.; Dwivedi, S.K. A review: The impact of hydrogen embrittlement on the fatigue strength of high strength steel. *Mater. Today Proc.* **2020**, *26*, 3015–3019. [CrossRef]

52. Hadi, M.S.; Saud, S.N.; Hamzah, E.; Mamat, M.F. Hydrogen embrittlement of 316L stainless steels exposed in 1.0M hydrochloric acid solution. *Ann. Chim. Sci. Matériaux* **2019**, *43*, 369–375. [CrossRef]

53. Xing, X.; Pang, Z.; Hao Zhang, H.; Liu, J.; Cui, G. Study of temperature effect on hydrogen embrittlement in X70 pipeline steel. *Corros. Sci.* **2024**, *230*, 111939. [CrossRef]

54. Sey, E.; Farhat, Z.N. Evaluating the Effect of Hydrogen on the Tensile Properties of Cold-Finished Mild Steel. *Crystals* **2024**, *14*, 529. [CrossRef]

55. Toribio, J. Hydrogen embrittlement of pearlitic steel in the presence of notches: A kinematic fracture criterion based on the notch tip strain rate. *Procedia Struct. Integr.* **2022**, *41*, 736–743. [CrossRef]

56. Badia, E.; Navajas, J.; Sala, R.; Paltrinieri, N.; Sato, H. Analysis of Hydrogen Value Chain Events: Implications for Hydrogen Refueling Stations' Safety. *Safety* **2024**, *10*, 44. [CrossRef]

57. Calabrese, M.; Portarapillo, M.; Di Nardo, A.; Venezia, V.; Turco, M.; Luciani, G.; Di Benedetto, A. Hydrogen Safety Challenges: A Comprehensive Review on Production, Storage, Transport, Utilization, and CFD-Based Consequence and Risk Assessment. *Energies* **2024**, *17*, 1350. [CrossRef]

58. Sinay, J.; Brestovič, T.; Markovič, J.; Glatz, J.; Gorzás, M.; Vargová, M. Analysis of the Risks of Hydrogen Leakage from Hydrogen-Powered Cars and Their Possible Impact on Automotive Market Share Increase. *Appl. Sci.* **2020**, *10*, 4292. [CrossRef]

59. Li, Q.; Ghadiani, H.; Jalilvand, V.; Alam, T.; Farhat, Z.; Islam, M.A. Hydrogen Impact: A Review on Diffusibility, Embrittlement Mechanisms, and Characterization. *Materials* **2024**, *17*, 965. [CrossRef] [PubMed]

60. Chaves, I.A.; Richardson, P.J.; Lynch, S.; Allen, J.A. Impact of the Delay Period between Electrochemical Hydrogen Charging and Tensile Testing on the Mechanical Properties of Mild Steel. *Corros. Mater. Degrad.* **2024**, *5*, 265–275. [CrossRef]

61. Ilyushechkin, A.; Schoeman, L.; Carter, L.; Hla, S.S. Material Challenges and Hydrogen Embrittlement Assessment for Hydrogen Utilisation in Industrial Scale. *Hydrogen* **2023**, *4*, 599–619. [CrossRef]

62. Ahad, M.T.; Bhuiyan, M.M.H.; Sakib, A.N.; Becerril Corral, A.; Siddique, Z. An Overview of Challenges for the Future of Hydrogen. *Materials* **2023**, *16*, 6680. [CrossRef]

63. Balitskii, A.I.; Havrilyuk, M.R.; Balitska, V.O.; Kolesnikov, V.O.; Ivaskevych, L.M. Increasing turbine hall safety by using fire-resistant, hydrogen-containing lubricant cooling liquid for rotor steel mechanical treatment. *Energies* **2023**, *16*, 535. [CrossRef]

64. Bhutta, M.U.; Najeeb, M.H.; Abdullah, M.U.; Shah, S.R.; Khurram, M.; Mufti, R.A.; Ogawa, K.; Aslam, J.; Zahid, R.; Ali, M.A.; et al. Experimental Investigation of Engine Valve Train Friction Considering Effects of Operating Conditions and WPC Surface Treatment. *Materials* **2023**, *16*, 3431. [CrossRef]

65. Sun, J.; Bai, L.; Guo, F.; Khan, Z.A. Experimental Study on the Effect of Micro-Texture on EHL Point-Contact Film Thickness Subject to Sliding Conditions. *Materials* **2022**, *15*, 7926. [CrossRef]

66. Li, C.-D.; Wang, J.-S.; Han, X.; Du, F.-M.; Liu, G.-S.; Lin, R.-J. Wear Performance of Circular Shim against Cam in Engine Bench Test. *Materials* **2022**, *15*, 6293. [CrossRef]

67. Żurawski, K.; Żurek, P.; Kawalec, A.; Bazan, A.; Olko, A. Modeling of Surface Topography after Milling with a Lens-Shaped End-Mill, Considering Runout. *Materials* **2022**, *15*, 1188. [CrossRef]

68. Bai, L.; Sun, J.; Zhang, P.; Khan, Z.A. Friction Behavior of a Textured Surface against Several Materials under Dry and Lubricated Conditions. *Materials* **2021**, *14*, 5228. [CrossRef] [PubMed]

69. Sawczuk, W.; Cañás, A.M.R.; Ulbrich, D.; Kowalczyk, J. Modeling the Average and Instantaneous Friction Coefficient of a Disc Brake on the Basis of Bench Tests. *Materials* **2021**, *14*, 4766. [CrossRef] [PubMed]

70. Liu, Y.; Zhang, H.; Dong, G. A Design of Partial Textured Surface on Gear Washers for Reducing Friction and Wear under Low Speed and Heavy Load Conditions. *Materials* **2021**, *14*, 4666. [CrossRef] [PubMed]

71. Wos, S.; Koszela, W.; Pawlus, P. Selected Methods and Applications of Anti-Friction and Anti-Wear Surface Texturing. *Materials* **2021**, *14*, 3227. [CrossRef]

72. Wang, W.; Zhao, W.; Liu, Y.; Zhang, H.; Hua, M.; Dong, G.; Tam, H.-Y.; Chin, K.-S. A Pocket-Textured Surface for Improving the Tribological Properties of Point Contact under Starved Lubrication. *Materials* **2021**, *14*, 1789. [CrossRef]

73. Lenart, A.; Pawlus, P.; Dzierwa, A.; Wos, S.; Reizer, R. The Effect of Surface Texture on Lubricated Fretting. *Materials* **2020**, *13*, 4886. [CrossRef]

74. Ran, H.; Liu, D.; Wang, S. A Numerical Wear Simulation Method of Reciprocating Seals with a Textured Rod. *Materials* **2020**, *13*, 4458. [CrossRef]

75. Qi, Y.; Sun, B.; Zhang, Y.; Gao, G.; Zhang, P.; Zheng, X. Study of Tribological Properties and Evolution of Morphological Characteristics of Transfer Films in PTFE Composites Synergistically Reinforced with Nano-ZrO_2 and PEEK Particles. *Polymers* **2023**, *15*, 3626. [CrossRef]

76. Liu, P.; Liu, J.; Gao, S.; Wang, Y.; Zheng, H.; Zhen, M.; Zhao, F.; Liu, Z.; Ou, C.; Zhuang, R. Calibration of Sliding Friction Coefficient in DEM between Different Particles by Experiment. *Appl. Sci.* **2023**, *13*, 11883. [CrossRef]

77. Li, Q.; Heß, M. Experimental Investigation of Frictional Resistance in Sliding Contact between Undulating Surfaces and Third-Body Particles. *Machines* **2024**, *12*, 150. [CrossRef]

78. Hagino, H.; Iwata, A.; Okuda, T. Iron Oxide and Hydroxide Speciation in Emissions of Brake Wear Particles from Different Friction Materials Using an X-ray Absorption Fine Structure. *Atmosphere* **2024**, *15*, 49. [CrossRef]

79. Zhao, Y.; Yang, G.; Wang, Z.; Yuan, S. Research on the Effect of Particle Size on the Interface Friction between Geogrid Reinforcement and Soil. *Sustainability* **2022**, *14*, 15443. [CrossRef]

80. Zhang, X.; Cao, Y.; Xue, B.; Hua, G.; Zhang, H. Method for Identifying Materials and Sizes of Particles Based on Neural Network. *J. Mar. Sci. Eng.* **2023**, *11*, 541. [CrossRef]

81. Yin, S.; Peng, T.; Yang, C.; Yang, C.; Gui, W.; Liu, L. Dynamic-Projection-Integrated Particle-Filtering-Based Identification of Friction Characteristic Curve for Train Wheelset on Slipping Fault Condition. *Lubricants* **2024**, *12*, 38. [CrossRef]

82. Di Maio, C.; Nunziati, G.; Mecocci, A. Deep-Learning-Based Action and Trajectory Analysis for Museum Security Videos. *Electronics* **2024**, *13*, 1194. [CrossRef]

83. Chen, Q.; Xiong, Q.; Huang, H.; Tang, S.; Liu, Z. Research on the Construction of an Efficient and Lightweight Online Detection Method for Tiny Surface Defects through Model Compression and Knowledge Distillation. *Electronics* **2024**, *13*, 253. [CrossRef]

84. Avianto, D.; Harjoko, A.; Afiahayati. CNN-Based Classification for Highly Similar Vehicle Model Using Multi-Task Learning. *J. Imaging* **2022**, *8*, 293. [CrossRef]

85. Patel, K.; Bhatt, C.; Mazzeo, P.L. Deep Learning-Based Automatic Detection of Ships: An Experimental Study Using Satellite Images. *J. Imaging* **2022**, *8*, 182. [CrossRef]

86. Sommerhoff, H.; Kolb, A. A Generic Framework for Depth Reconstruction Enhancement. *J. Imaging* **2022**, *8*, 138. [CrossRef]

87. Yerram, V.; Takeshita, H.; Iwahori, Y.; Hayashi, Y.; Bhuyan, M.K.; Fukui, S.; Kijsirikul, B.; Wang, A. Extraction and Calculation of Roadway Area from Satellite Images Using Improved Deep Learning Model and Post-Processing. *J. Imaging* **2022**, *8*, 124. [CrossRef]

88. Hu, G.; Dixit, C.; Qi, G. Discriminative Shape Feature Pooling in Deep Neural Networks. *J. Imaging* **2022**, *8*, 118. [CrossRef] [PubMed]

89. El Shair, Z.; Rawashdeh, S.A. High-Temporal-Resolution Object Detection and Tracking Using Images and Events. *J. Imaging* **2022**, *8*, 210. [CrossRef] [PubMed]

90. Gao, M.; Zou, G.; Li, Y.; Guo, X. Recent Advances in Computer Vision: Technologies and Applications. *Electronics* **2024**, *13*, 2734. [CrossRef]

91. Wang, J.-Y.; Liu, S.-K.; Guo, S.-C.; Jiang, C.-Y.; Zheng, W.-M. PCNet: Leveraging Prototype Complementarity to Improve Prototype Affinity for Few-Shot Segmentation. *Electronics* **2024**, *13*, 142. [CrossRef]

92. Yu, Q.; Zhu, G. Digital Restoration and 3D Virtual Space Display of Hakka Cardigan Based on Optimization of Numerical Algorithm. *Electronics* **2023**, *12*, 4190. [CrossRef]

93. Available online: http://base.uipv.org/searchINV/search.php?action=viewdetails&IdClaim=225530 (accessed on 17 October 2024).

94. Gonsales, R.S.; Woods, R.; Eddins, S. *Digital Image Processing using MATLAB*; Pearson Education: London, UK, 2004; p. 620. ISBN 8177588982, 9788177588989. Available online: https://www.cin.ufpe.br/~sbm/DEN/Digital%20Image%20Processing%20Using%20Matlab%20(Gonzalez).pdf (accessed on 17 October 2024).

95. Forsyth, D.; Ponce, J. *Computer Vision: A Modern Approach*, 2nd ed.; Prentice Hall: Hoboken, NJ, USA, 2011.

96. Horn, B.K.P. *Robot Vision*; MIT Press: Cambridge, MS, USA; McGraw-Hill: New York City, NY, USA, 1986; p. 509. ISBN 9780262537377.

97. Ikeuchi, K.; Horn, B.K.P. Numerical shape from shading and occluding boundaries. *Artif. Intell.* **1981**, *17*, 141–184. [CrossRef]

98. Kolesnikov, V.; Balytskyi, O.; Havryliuk, M.; Ivaskevych, L. Image Processing of Wear Products and Cutting of High-Strength Steels And Alloys, Certificate of Copyright Registration and Work No. 101853, 15 January 2021. Available online: https://ukrpatent.org/atachs/buleten-avt-pravo-63-2021-01.zip (accessed on 17 October 2024).

99. Simmons, J.W. Overview: High-nitrogen alloying of stainless steels. *Mater. Sci. Eng. A* **1996**, *207*, 159–169. [CrossRef]

100. Gavriljuk, V.G.; Berns, H. *High Nitrogen Steels–Structure, Properties, Manufacture. Applications*; Springer Science & Business Media: Berlin, Germany, 1999; p. 378.

101. Thomann, U.I.; Uggowitzer, P.J. Wear–corrosion behavior of bio compatible austenitic stainless steels. *Wear* **2000**, *239*, 48–58. Available online: https://www.sciencedirect.com/science/article/abs/pii/S0043164899003725?via=ihub (accessed on 17 October 2024). [CrossRef]

102. Büscher, R.; Fischer, A. Sliding wear behaviour of an electrochemically modified austenitic high-nitrogen steel surface. *Wear* **2003**, *254*, 1318–1325. [CrossRef]

103. Stein, G.; Hucklenbroich, I. Manufacturing and Applications of High Nitrogen Steels. *Mater. Manuf. Process.* **2004**, *19*, 7–17. [CrossRef]

104. Bregliozzi, G.; Schino, A.D.; Ahmed, S.I.-U. Cavitation wear behaviour of austenitic stainless steels with different grain sizes. *Wear* **2005**, *258*, 503–510. [CrossRef]

105. Speidel, M.O. Nitrogen containing austenitic stainless steels. *Materwiss Werksttech* **2006**, *37*, 875–880. [CrossRef]

106. Li, H.; Jiang, Z.; Zhang, Z.; Xu, B.; Liu, F. Mechanical Properties of Nickel Free High Nitrogen Austenitic Stainless Steels. *J. Iron Steel Res. Int.* **2007**, *14*, 330–334. [CrossRef]

107. Mesa, D.H.; Garzón, C.M.; Tschiptschin, A.P. Influence of cold-work on the cavitation erosion resistance and on the damage mechanisms in high-nitrogen austenitic stainless steels. *Wear* **2011**, *271*, 1372–1377. [CrossRef]

108. Saenarjhan, N.; Kang, J.-H.; Kim, S.-J. Effects of carbon and nitrogen on austenite stability and tensile deformation behavior of 15Cr-15Mn-4Ni based austenitic stainless steels. *Mater. Sci. Eng. A* **2019**, *742*, 608–616. [CrossRef]

109. Liu, P.; Chu, Z.K.; Yuan, Y. Microstructures and Mechanical Properties of a Newly Developed Austenitic Heat Resistant Steel. *Acta Metall. Sin.* **2019**, *32*, 517–525. [CrossRef]

110. Ferreira, V.H.M.M.; Coury, F.G.; de Araujo Santana, D.; Kogaz, G.Y. Novel high nitrogen austenitic stainless steels: From high-throughput screening to experimental validation and properties relationship. *J. Mater. Res. Technol.* **2024**, *30*, 640–656. [CrossRef]

111. Balitskii, A.I.; Syrotyuk, A.M.; Havrilyuk, M.R.; Balitska, V.O.; Kolesnikov, V.O.; Ivaskevych, L.M. Hydrogen Cooling of Turbo Aggregates and the Problem of Rotor Shafts Materials Degradation Evaluation. *Energies* **2023**, *16*, 7851. [CrossRef]

112. Balyts'kyi, O.I.; Kolesnikov, V.O.; Havrylyuk, M.R. Influence of lubricating liquid on the formation of the products of cutting of 38KhN3MFA steel. *Mater. Sci.* **2019**, *54*, 722–727. [CrossRef]

113. Balyts'kyi, O.I.; Kolesnikov, V.O.; Havrylyuk, M.R. Influence of modification of 38KhN3MFA steel on the structural-phase state and cutting products under variable technological conditions. *Mater. Sci.* **2020**, *55*, 915–920. [CrossRef]

114. Balyts'kyi, O.I.; Kolesnikov, V.O.; Kubicki, E. Enhancement of the crack resistance of manganese cast irons. *Mater. Sci.* **2005**, *41*, 67–73. [CrossRef]

115. Balitskii, A.; Kolesnikov, V.; Abramek, K.F.; Balitskii, O.; Eliasz, J.; Havrilyuk, M.; Ivaskevych, L.; Kolesnikova, I. Influence of hydrogen-containing fuels and environmentally friendly lubricating coolant on nitrogen steels wear resistance for spark ingnition engine pistons and rings kit gasket set. *Energies* **2021**, *14*, 7583. [CrossRef]

116. Balitskii, A.; Kindrachuk, M.; Volchenko, D.; Abramek, K.F.; Balitskii, O.; Skrypnyk, V.; Zhuravlev, D.; Bekish, I.; Ostashuk, M.; Kolesnikov, V. Hydrogen containing nano fluids in the spark engine's cylinder head cooling system. *Energies* **2022**, *15*, 59. [CrossRef]

117. Balitskii, A.A.; Kolesnikov, V.A.; Vus, O.B. Tribotechnical properties of nitrogen manganese steels under rolling friction at addition of $(GaSe)_x In_{1-x}$ powders into contact zone. *Metallofiz. Noveishie Tekhnologii* **2010**, *32*, 685–695.

118. Balyts'kyi, O.I.; Kolesnikov, V.O.; Kawiak, P. Triboengineering properties of austenitic manganese steels and castirons under the conditions of sliding friction. *Mater. Sci.* **2005**, *41*, 624–630. [CrossRef]

119. Kindrachuk, M.; Volchenko, D.; Balitskii, A.; Abramek, K.F.; Volchenko, M.; Balitskii, O.; Skrypnyk, V.; Zhuravlev, D.; Yurchuk, A.; Kolesnikov, V. Wear resistance of spark ignition engine piston rings in hydrogen-containing environments. *Energies* **2021**, *14*, 4801. [CrossRef]

120. Balitskii, O.I.; Kolesnikov, V.O.; Ivaskevych, L.M.; Havrylyuk, M.R. The Influence of Specific Features of Load and Hydrogen Charging on Steel Tribotechnical Properties. *Mater. Sci.* **2023**, *58*, 502–512. [CrossRef]

121. Balitskii, O.A.; Kolesnikov, V.O.; Balitskii, A.I.; Eliasz, J.J.; Havrylyuk, M.R. Hydrogen effect on the high-nickel surface steel properties during machining and wear with lubricants. *Arch. Mater. Sci. Eng.* **2020**, *104*, 49–57. [CrossRef]

122. Glotka, O.A.; Haiduk, S.V. Distribution of elements in carbides of multicomponent superalloys. *Metallofiz. Noveishie Tekhnol.* **2020**, *42*, 869–884. [CrossRef]

123. Glotka, A.A.; Moroz, A.N. Comparison of the effects of carbides and nonmetallic inclusions on formation of fatigue microcracks in steels. *Metal Sci. Heat Treat.* **2019**, *61*, 521–524. [CrossRef]

124. Trzepieciński, T.; Szwajka, K.; Szewczyk, M.; Barlak, M.; Zielińska-Szwajka, J. Effect of Countersample Coatings on the Friction Behaviour of DC01 Steel Sheets in Bending-under-Tension Friction Tests. *Materials* **2024**, *17*, 3631. [CrossRef] [PubMed]

125. Czapla, K.; Żaba, K.; Kot, M.; Nejman, I.; Madej, M.; Trzepieciński, T. Tribological Performance of Anti-Wear Coatings on Tools for Forming Aluminium Alloy Sheets Used for Producing Pull-Off Caps. *Materials* **2023**, *16*, 6465. [CrossRef] [PubMed]

126. Kyryliv, V.; Maksymiv, O.; Gurey, V.; Hurey, I.; Kyryliv, Y.; Zvirko, O. The mode deformation effect on surface nanocrystalline structure formation and wear resistance of steel 41Cr4. *Coatings* **2023**, *13*, 249. [CrossRef]

127. Nykyforchyn, H.; Kyryliv, V.; Maksymiv, O.; Zvirko, O. Mechanical fabrication methods of nanostructured surfaces. In *Handbook of Modern Coating Technologies. Fabrication Methods and Functional Properties*; Aliofkhazraei, M., Ali, N., Chipara, M., Laidani, N.B., De Hosson, J.T.M., Eds.; Elsevier: Amsterdam, The Netherlands, 2021; pp. 25–67. [CrossRef]

128. Khoma, M.S.; Korniy, S.A.; Vynar, V.A.; Datsko, B.M.; Maksishko, Y.; Dykha, O.V.; Bukliv, R.L. Influence of hydrogen sulfide on the carbon-dioxide corrosion and the mechanical characteristics of high-strength pipe steel. *Mater. Sci.* **2022**, *1*, 805–812. [CrossRef]

129. Pokhmurs'kyi, V.I.; Vasyliv, K.B. Influence of hydrogen on the friction and wear of metals (a survey). *Mater. Sci.* **2012**, *48*, 125–138. [CrossRef]

130. Chernousenko, O.; Rindyuk, D.; Peshko, V.; Bednarska, I. Effect of Start-Up Operating Modes on the Cyclic Damage of Thermal Power Plant Units. In Proceedings of the 2022 IEEE 8th International Conference on Energy Smart Systems (ESS), Kyiv, Ukraine, 7–9 September 2022; pp. 233–238. [CrossRef]

131. Hembara, O.V.; Chepil, O.Y.; Hembara, N.T.; Syrotyuk, A.M. Evaluation of the Influence of the Hydrogenation of Metal on the Durability of Heat-Exchanger Tubes of Steam Generators. *Mater. Sci.* **2022**, *58*, 325–330. [CrossRef]

132. Bovsunovsky, A.; Shtefan, E.; Peshko, V. Modeling of the circumferential crack growth under torsional vibrations of steam turbine shafting. *Theor. Appl. Fract. Mech.* **2023**, *2023*, 103881. [CrossRef]

133. Yasniy, P.V.; Okipnyi, I.B.; Maruschak, P.O.; Panin, S.V.; Konovalenko, I.V. Crack tip strain localisation on mechanics of fracture of heat resistant steel after hydrogenation. *Theor. Appl. Fract. Mech.* **2013**, 63–68. [CrossRef]

134. Onysko, O.; Kopei, V.; Vytvytskyi, V.; Vriukalo, V.; Lukan, T. Calculation of the accuracy of the drill-string nc13 thread profile turned from difficult-to-machine steel. *Lect. Notes Mech. Eng.* **2024**, 182–192. [CrossRef]

135. Tkach, P.; Reviakina, O.; Kryvosheia, A.; Ustynenko, O.; Protasov, R. Meshing characteristics of profile shifted cylindrical quasi-involute arc-tooth-trace gears. Part 1. *Theor. Base. Stroj. Casopis.* **2022**, *72*, 201–210. [CrossRef]

136. Terniuk, M.E.; Kryvosheia, A.V.; Krasnoshtan, A.M.; Tkach, P.M.; Lutskii, S.V. Gear manufacturing accuracy prediction, control, and management. In *Novikov/Conform. Gearing*; Springer: Berlin/Heidelberg, Germany, 2023; pp. 215–323. [CrossRef]

137. Andreikiv, O.Y.; Dolins'ka, I.Y.; Shtoiko, I.P.; Raiter, O.K.; Matviiv, Y.Y. Evaluation of the residual service life of main pipelines with regard for the action of media and degradation of materials. *Mater. Sci.* **2019**, *54*, 638–646. [CrossRef]

138. Onysko, O.; Kopei, V.; Medvid, I.; Panchuk, V.; Pituley, L.; Vryukalo, V. Analytical investigations of the accuracy of the small diameter tool-joint tapered thread made by a lathe machining. *New Trends Prod. Eng.* **2019**, *2*, 1. [CrossRef]

139. Permyakov, A.; Dobrotvorskiy, S.; Dobrovolska, L.; Basova, Y.; Ivanova, M. Computer modeling application for predicting of the passing of the high-speed milling machining hardened steel. In *Advances in Design, Simulation and Manufacturing*; Springer: Berlin/Heidelberg, Germany, 2019; DSMIE, Lecture Notes in Mechanical Engineering. [CrossRef]

140. Santone, A.; De Vivo, R.; Recchia, L.; Cesarelli, M.; Mercaldo, F. A Method for Retina Segmentation by Means of U-Net Network. *Electronics* **2024**, *13*, 4340. [CrossRef]

141. Zhang, Y.; Chu, J.; Leng, L.; Miao, J. Mask-Refined R-CNN: A Network for Refining Object Details in Instance Segmentation. *Sensors* **2020**, *20*, 1010. [CrossRef]

142. Wang, H.; Liu, J.; Huang, C.; Yang, X.; Hu, D.; Chen, L.; Xing, X.; Jiang, Y. Semi-Supervised Instance-Segmentation Model for Feature Transfer Based on Category Attention. *Sensors* **2022**, *22*, 8794. [CrossRef]

143. Terven, J.; Córdova-Esparza, D.-M.; Romero-González, J.-A. A Comprehensive Review of YOLO Architectures in Computer Vision: From YOLOv1 to YOLOv8 and YOLO-NAS. *Mach. Learn. Knowl. Extr.* **2023**, *5*, 1680–1716. [CrossRef]

144. Moksyakov, A.; Wu, Y.; Gadsden, S.A.; Yawney, J.; AlShabi, M. Object Detection and Tracking with YOLO and the Sliding Innovation Filter. *Sensors* **2024**, *24*, 2107. [CrossRef]

145. Karathanasopoulos, N.; Hadjidoukas, P. Deep learning based automated fracture identification in material characterization experiments. *Adv. Eng. Inform.* **2024**, *60*, 102402. [CrossRef]

146. Bastidas-Rodriguez, M.X.; Polania, L.; Gruson, A.; Prieto-Ortiz, F. Deep Learning for fractographic classification in metallic materials. *Eng. Fail. Anal.* **2020**, *113*, 104532. [CrossRef]

147. Engelhardt, A.; Decke, J.; Meier, D.; Dulig, F.; Ragunathan, R.; Wegener, T.; Sick, B.; Niendorf, T. On the Reliability of Automated Analysis of Fracture Surfaces Using a Novel Computer Vision-Based Tool. *Adv. Eng. Mater.* **2023**, *25*, 2300876. [CrossRef]

148. Stachowiak, G.P.; Stachowiak, G.W.; Podsiadlo, P. Automated classification of wear particles based on their surface texture and shape features. *Tribol. Int.* **2008**, *41*, 34–43. [CrossRef]

149. He, L.; Wei, H.; Gao, W. Research on an Intelligent Classification Algorithm of Ferrography Wear Particles Based on Integrated ResNet50 and SepViT. *Lubricants* **2023**, *11*, 530. [CrossRef]

150. Wong, J.; Wei, H.; Zhou, D.; Cao, Z. The Target Detection of Wear Particles in Ferrographic Images Based on the Improved YOLOv8. *Lubricants* **2024**, *12*, 280. [CrossRef]

151. He, L.; Wei, H.; Wang, Q. A New Target Detection Method of Ferrography Wear Particle Images Based on ECAM-YOLOv5-BiFPN Network. *Sensors* **2023**, *23*, 6477. [CrossRef]